JOURNAL OF SOLID STATE CHEMISTRY **135,** 312–321 (1998)
ARTICLE NO. SC977652

Structure Analysis of the 6H–Ba(Ti, Fe^{3+}, Fe^{4+})$O_{3-\delta}$ Solid Solution

Ian E. Grey,* Christina Li,* Lachlan M. D. Cranswick,* Robert S. Roth,† and Terrell A. Vanderah†

* *CSIRO Division of Minerals, Clayton, Victoria 3168, Australia; and* † *National Institute of Standards and Technology, Ceramics Division, Gaithersburg, Maryland 20899*

Received May 8, 1997; in revised form September 23, 1997; accepted October 7, 1997

The 6H form of $BaTiO_3$ forms an extensive solid solution with barium iron oxide, having the general formula $BaTi_{1-x-y}Fe^{3+}_xFe^{4+}_yO_{3-x/2}$, where the Fe^{3+}/Fe^{4+} ratio depends on reaction temperature and gas atmosphere. Two series of solid solutions with iron predominantly in the form Fe^{3+} or Fe^{4+} were prepared by quenching from high temperatures in air or slow cooling to 200°C in oxygen, respectively. The structural variations in both series were obtained from Rietveld refinements of powder X-ray diffraction data. For the series with $y \sim 0$, the progressive substitution of Ti^{4+} by Fe^{3+} is accompanied by the formation of O(1) oxygen vacancies in the *h*-BaO_3 layers that separate pairs of occupied face-shared octahedra. The maximum vacancy concentration occurs at $x = 0.67$, which corresponds to a composition of $Ba\square O_2$ ($\square$ = vacancy) in the *h*-stacked layers. Solid solution members with $x > 0.67$ were unstable relative to other polymorphs. Further incorporation of iron into the 6H structure at high temperature occurs by substitution of Ti^{4+} by Fe^{4+}, i.e., by increasing *y*. The observed structural variations in the solid solution phases are explained in terms of the Ba and Fe, Ti atom packing and the changes in interatomic interactions between the metal atoms as oxygen is removed from the O(1) site. © 1998 Academic Press

INTRODUCTION

The system $BaO–Fe_2O_3–TiO_2$ offers materials scientists the exciting inducement that new phases can be prepared combining the high dielectric properties of the barium titanates with the strongly magnetic properties of the barium ferrites. A detailed study of subsolidus phase relations in this ternary system at 1250–1270°C in air (1) has recently been reported. The system was found to be complex, containing at least sixteen ternary compounds, of which the majority were new structure types, and an extensive solid solution between $BaTiO_3$ and $BaFeO_{2.5}$ with the hexagonal 6H–$BaTiO_3$ structure. The latter was studied using powder X-ray diffraction (PXRD) methods. The unit cell parameters for the solid solution members showed a nonlinear compositional dependence, with the *c* parameter passing through a maximum at about 40 mol% of the iron component. This was attributed to competing structural effects involving the formation of oxygen vacancies and the partial oxidation of iron to the tetravalent state at higher iron contents.

To gain further insight into the structural processes operating in the 6H phases, two solid solution series in which the iron was predominantly either trivalent or tetravalent were prepared. Rietveld refinements using PXRD data collected on the members of each solid solution were made to determine the structure variations as a function of composition. We present here the results of the phase studies and structure analyses for the two solid solutions. A detailed analysis of the accuracy of PXRD refinements from a comparative study of the results of multiple PXRD refinements and powder neutron diffraction refinements for the composition $BaFe_{0.667}Ti_{0.333}O_{3-\delta}$ will be reported elsewhere (2).

THE 6H–$BaTiO_3$ STRUCTURE

The crystal structure of the 6H form of $BaTiO_3$ was first published by Burbank and Evans (3). A more precise refinement has been reported by Akimoto *et al.* (4) on pure single crystals with cell parameters $a = 5.7238(7)$ Å and $c = 13.9649(7)$ Å, and space group $P6_3/mmc$. The structure is illustrated in Fig. 1. It is built of six closest-packed layers of composition BaO_3, arranged in the stacking sequence ABCBAC ($\equiv$ *chcchc* …). Ti(2) atoms occupy pairs of octahedra that share a common face across the *h*-stacked $Ba(1)O(1)_3$ layers. A second type of octahedrally coordinated titanium site, Ti(1), is situated between pairs of *c*-stacked $Ba(2)O(2)_3$ layers. The $Ti(2)_2O_9$ groups and $Ti(1)O_6$ octahedra are linked via corner-sharing. The Ti(2)–Ti(2) separation is 2.690(4) Å (4).

EXPERIMENTAL

Syntheses and Characterization

Starting materials for the preparations were analytical reagent grade $BaCO_3$, Fe_2O_3, and TiO_2. Weighed mixtures of the three components were homogenized by grinding in acetone. The mixtures were given two 30-min. heats at

0022-4596/98 $25.00

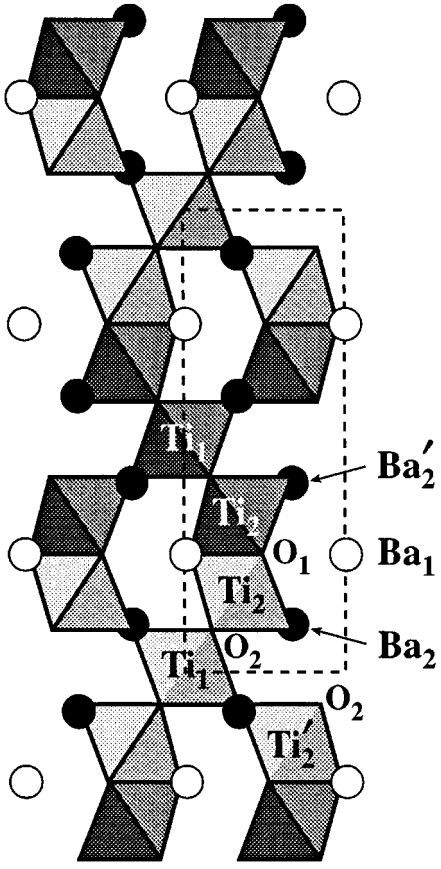

FIG. 1. Structure for $BaTiO_3$, viewed along [110]. Large open and filled circles correspond to Ba(1) and Ba(2) respectively. Atom labels and primed labels match the corresponding labels in Figs. 4–6.

900°C with intermediate grinding to decompose the carbonate. They were then pressed into pellets for further heat treatments.

In an earlier study (1), members of the 6H solid solution were prepared by multiple heatings in air at 1250–1270°C, followed by step-cooling to 750°C, then air quenching. Qualitative tests showed that the products contained variable amounts of Fe^{3+} and Fe^{4+}. In view of the rapid kinetics of iron oxidation/reduction (demonstrated in our laboratory by thermogravimetric studies), the products obtained are considered to correspond to equilibrium in air at 750°C.

In the current study, solid solution members with the iron predominantly in the trivalent state, $BaTi_{1-x}Fe_xO_{3-x/2}$, were prepared by heating the pelleted prereacted mixtures in air at high temperature for 16 to 20 h, then quenching in liquid nitrogen. The samples were given multiple heat treatments with intermediate fine grinding until powder X-ray diffraction patterns on successive samples showed no changes. The preparation temperature was varied for different compositions to avoid the formation of second phases. At $x = 0.125$, a temperature at 1400°C was employed to avoid the formation of tetragonal $BaTiO_3$ as a second phase. A temperature of 1200°C was suitable for samples with $0.2 < x < 0.67$. For compositions with $x > 0.67$, the 6H phase was not stable at 1200°C. As the [Fe]/[Fe + Ti] ratio increased above 0.67, the reaction temperature had to be progressively decreased to obtain a single phase 6H product free from other $BaFeO_{3-\delta}$ polymorphs. At $x = 0.8$, for example, it was necessary to decrease the temperature to 950°C, and at $x = 1$ a temperature of 800°C was used.

Solid solution members with the majority of the iron in the tetravalent state, ideally $BaTi_{1-y}Fe_yO_3$, were prepared by reheating samples from the first series to their preparation temperature in a tube furnace and then step-cooling the samples to 200°C over 3 h in a flow of oxygen. The samples were held at 200°C for period of 5 to 20 h, then cooled quickly in oxygen to room temperature.

The weights of the samples before and after slow cooling in oxygen, and also before and after reheating the slow-cooled samples in air to the original reaction temperatures, were carefully monitored. Direct analyses for tetravalent iron were made by dissolving the samples in a 3 M HCl solution saturated with carbon dioxide that contained an excess of AR ferrous sulfate solution, then titrating the solution against a standard solution of potassium dichromate. It was found that the titration method gave low results for tetravalent iron in the $BaFeO_{3-\delta}$ samples when compared with the composition vs lattice parameter curves obtained by Mori (5). An alternative analytical method used for determining oxygen content, and thereby Fe^{4+}/Fe^{3+}, was to heat the sample to constant weight in high purity argon at 1100°C, to convert all iron quantitatively to Fe^{3+} (5). The Fe^{4+} content was calculated from the measured weight decrease.

X-ray Data Collections and Rietveld Analyses

X-ray intensity data on ball-milled single-phase samples were collected on a Philips 1050/1710 diffractometer fitted with a graphite monochromator in the diffracted beam and employing Cu$K\alpha$ radiation. The X-ray tube was operated at 40 kV and 40 mA, with a 1° divergence slit, a 0.2-mm receiving slit, a 1° scatter slit, and Soller slits in the incident and diffracted beams. Step-scan intensity measurements in the 2θ range 10 to 150° were made at intervals of 0.025°. A variable step-counting time strategy (6) that increases the counting time with diffraction angle in a manner inversely proportional to the intensity fall-off from factors such as Lorentz polarization, element scattering factors, and thermal parameters was used. This results in a relatively uniform intensity distribution over the full angular range with corresponding uniform weighting. The total counting time was typically 30 ksec. Least-squares structure refinements were carried out using the Rietveld program CSRIET/SR5,

a local modification of the code by Hill and Howard (7) and Wiles and Young (8) that takes account of variable-time data sets. Profile refinement parameters included a scale factor, pseudo-Voigt peak shape parameters, a peak full-width at half maximum (FWHM) function (9) of the form $\mathrm{FWHM}^2 = U\tan 2\theta + V\tan\theta + W$, a 2θ zero parameter, and the unit cell parameters. The background was refined using a four-parameter polynomial in $2\theta n$, where n has values from 0 to 3, inclusive. X-ray scattering factors for ionized atoms, including anomolous dispersion, were taken from the "International Tables for X-Ray Crystallography" (10).

Refinements were initiated using the published coordinates (4) for 6H $BaTiO_3$ in space group $P6_3/mmc$. The iron and titanium atoms were statistically distributed over the two independent metal atom sites, consistent with the results of a powder neutron refinement for one of the compositions (2). For the high-temperature quenched samples, the refined atomic displacement parameters were normal for the O(2) oxygen sites in the cubic-packed layers but very high (B typically 5–10 Å^2) for the O(1) oxygen sites in the hexagonal-packed layers. Subsequent refinements of site occupancy fractions (SOF) for the O(1) and O(2) sites confirmed that anion vacancies were confined to the O(1) sites. Attempts to refine Bs and SOFs simultaneously for the O(1) site were not successful because of the very flat R-factor minimum as a function of these two variables. The refinements were completed by fixing the B value for O(1) to 1.5 Å^2 and refining the SOF for this site. The B value 1.5 Å^2 is consistent with the value 1.7(2) Å^2 reported by Jacobson (11) from a neutron diffraction refinement for $BaFeO_{2.79}$. In test refinements with different fixed values of B for O(1), we found that the refined SOF for O(1) varied by 0.01 per 0.5 Å^2 change in B.

RESULTS AND DISCUSSION

Rietveld refinement results for quenched samples containing iron predominantly as Fe^{3+} are given in Table 1, and results for samples slow cooled in oxygen, with Fe^{4+} as the major iron species, are reported in Table 2.

Cell Parameter Variations

The unit cell parameters are plotted as a function of the [Fe]/[Fe + Ti] atomic ratio in Fig. 2. The straight lines

TABLE 1
Rietveld Refinement Results for Quenched Samples

[Fe]/[Ti + Fe]	0.125	0.25	0.364	0.50	0.667 fresh	0.667 aged 4 months	0.800	0.900	1.0
$[Fe^{4+}]/[Fe_{tot}]$				0.05	0.03		0.19		0.36
a (Å)	5.7260(1)	5.7263(1)	5.7274(1)	5.7288(1)	5.7303(1)	5.7248(2)	5.7229(1)	5.7155(2)	5.6985(1)
c (Å)	14.0114(1)	14.0597(1)	14.1012(1)	14.1444(1)	14.1870(2)	14.4355(7)	14.1638(3)	14.1353(5)	14.0464(4)
Ba(1) (2*b*)									
B (Å^2)	0.56(2)	0.65(2)	0.65(2)	0.70(3)	0.99(3)	0.90(6)	0.87(4)	0.75(5)	0.61(3)
Ba(2) (4*f*)									
z	0.09553(7)	0.09389(6)	0.09246(6)	0.09076(9)	0.0892(1)	0.0834(1)	0.0881(1)	0.0871(1)	0.0856(1)
B (Å^2)	0.73(2)	0.81(2)	0.80(2)	0.96(2)	1.20(2)	1.77(5)	1.20(3)	1.21(4)	0.74(3)
M(1) (2*a*)									
B (Å^2)	0.50(6)	0.45(6)	0.38(5)	0.67(7)	0.75(7)	0.2(1)	1.19(9)	0.64(9)	0.64(7)
M(2) (4*f*)									
z	0.8486(2)	0.8495(2)	0.8508(2)	0.8524(2)	0.8538(2)	0.8545(4)	0.8530(2)	0.8529(3)	0.8507(2)
B (Å^2)	0.75(5)	0.98(5)	0.96(5)	0.84(6)	1.30(6)	1.6(1)	1.09(8)	1.5(1)	0.74(7)
O(1) (6*h*)									
x	0.520(1)	0.518(1)	0.519(1)	0.520(1)	0.522(2)	0.514(2)	0.522(2)	0.522(2)	0.524(2)
B (Å^2)	1.5	1.5	1.5	1.5	1.5	1.5	1.5	1.5	1.5
SOF	0.230(5)	0.222(6)	0.201(5)	0.184(6)	0.160(6)	0.181(5)	0.169(7)	0.176(7)	0.174(7)
O(2) (12*k*)									
x	0.8340(9)	0.8337(8)	0.8327(8)	0.836(1)	0.8364(9)	0.835(1)	0.837(1)	0.836(1)	0.832(1)
z	0.0815(4)	0.0815(4)	0.0816(4)	0.0822(4)	0.0817(4)	0.0811(6)	0.0828(5)	0.0829(6)	0.0833(6)
B (Å^2)	0.3(1)	0.33(8)	0.45(8)	0.5(1)	0.7(1)	1.3(2)	0.8(1)	1.5(2)	1.2(1)
R_{wp}	12.1	11.4	11.2	14.0	11.6	16.5	14.0	13.8	12.7
R_B	2.9	4.1	5.7	6.0	4.0	5.9	5.2	6.1	3.9

TABLE 2
Rietveld Refinement Results for Samples Slow-Cooled in Oxygen

[Fe]/[Ti + Fe]	0.0 (Ref. 4)	0.200	0.500	0.667	0.800	1.00
$[Fe^{4+}]/[Fe_{tot}]$		0.63	0.67	0.75	0.79	0.87
a (Å)	5.7238(7)	5.7179(1)	5.7034(1)	5.6914(1)	5.6821(1)	5.6707(1)
c (Å)	13.9649(7)	13.9836(1)	13.9797(2)	13.9518(1)	13.9392(2)	13.9039(2)
Ba(1) (2*b*)						
B (Å^2)	0.43	0.55(2)	0.47(2)	0.38(2)	0.36(2)	0.44(2)
Ba(2) (4*f*)						
z	0.09671(5)	0.09524(6)	0.09230(8)	0.09127(7)	0.09031(7)	0.08974(9)
B (Å^2)	0.52	0.64(2)	0.55(2)	0.46(2)	0.50(2)	0.54(2)
M(1) (2*a*)						
B (Å^2)	0.67	0.59(6)	0.45(6)	0.32(5)	0.30(5)	0.36(5)
M(2) (4*f*)						
z	0.8463(1)	0.8472(2)	0.8473(2)	0.8473(2)	0.8474(2)	0.8467(2)
B (Å^2)	0.62	0.57(5)	0.48(5)	0.19(4)	0.29(5)	0.49(5)
O(1) (6*h*)						
x	0.5185(6)	0.5185(9)	0.519(1)	0.5198(9)	0.520(1)	0.521(1)
B (Å^2)	0.65	1.1(1)	1.5(2)	0.8(1)	1.1(2)	1.4(2)
SOF	0.25	0.25	0.25	0.25	0.25	0.25
O(2) (12*k*)						
x	0.8349(6)	0.8335(9)	0.835(1)	0.8324(9)	0.833(1)	0.832(1)
z	0.0802(2)	0.0814(4)	0.0823(5)	0.0830(4)	0.0829(4)	0.0826(5)
B (Å^2)	0.66	0.35(8)	0.4(1)	0.6(1)	0.7(1)	0.5(1)
R_{wp}		12.3	13.6	11.7	10.8	12.2
R_B	3.7	3.9	4.5	3.2	3.8	2.6

shown in Fig. 2 represent the expected cell parameter changes for the $BaTiO_3$–$BaFeO_3$ and $BaTiO_3$–$BaFeO_{2.5}$ solid solutions based on Vegard's law being obeyed. The parameters for the two barium iron oxide end members were obtained by extrapolating the linear cell parameter–composition relationships presented by Mori (5) in his study on 6H–$BaFeO_{3-\delta}$ compositions with $0.08 \leq \delta \leq 0.37$.

Figure 2 shows that the cell parameter trends for the quenched phases undergo major changes at a [Fe]/[Fe + Ti] raio of 0.67. These changes correlate with abrupt changes in the O(1) SOF variations and the Fe^{4+} content of the quenched phases for [Fe]/[Fe + Ti] > 0.67, as shown by the results in Table 1. For the slow-cooled samples, the plots of the *a* and *c* parameters vs [Fe]/[Fe + Ti] are approximately parallel to the Vegard law lines for $BaTiO_3$–$BaFeO_3$, but they are displaced to higher values. This is consistent with the results of chemical analyses, given in Table 2, which show that an appreciable proportion of the iron is retained as Fe^{3+} after slow cooling in oxygen.

Oxygen Vacancies

The refined SOF for O(1) is plotted vs the [Fe]/[Fe + Ti] ratio in Fig. 3. The SOF decreases linearly as the iron atomic fraction is increased from 0.0 to 0.67, then remains approximately constant for [Fe]/[Fe + Ti] values between 0.67 and 1.0. Within the experimental errors, the results for [Fe]/[Fe + Ti] values in the range 0.0 to 0.67 are fitted by a line calculated for the $BaTiO_3$–$BaFeO_{2.5}$ solid solution, assuming that the oxygen vacancies are confined to the O(1) site. According to this model, the composition with [Fe]/[Fe + Ti] = 0.67 has one oxygen in three missing in the layers containing O(1), giving a composition for the *h*-stacked layers of Ba□O_2 (□ = vacancy) and an overall composition of $Ba(Fe_{0.67}Ti_{0.33})O_{2.67}$. The results in Fig. 3 show that this is the maximum vacancy concentration that could be achieved for the treatments in air used in this study. Attempts to introduce higher vacancy concentrations (higher Fe^{3+} contents) by heating compositions with [Fe]/[Fe + Ti] > 0.67 to higher temperatures resulted in conversion of the 6H phase to phases with XRD patterns similar to the triclinic I phase reported by Mori (5).

At [Fe]/[Fe + Ti] ratios greater than 0.67, the O(1) SOF increases slightly with increasing iron content. Although the changes are barely significant, they are consistent for successive samples, and when considered in relation to the associated increases in the B values for O(2) shown in Table 2 (see Table 1), they suggest that there may be a

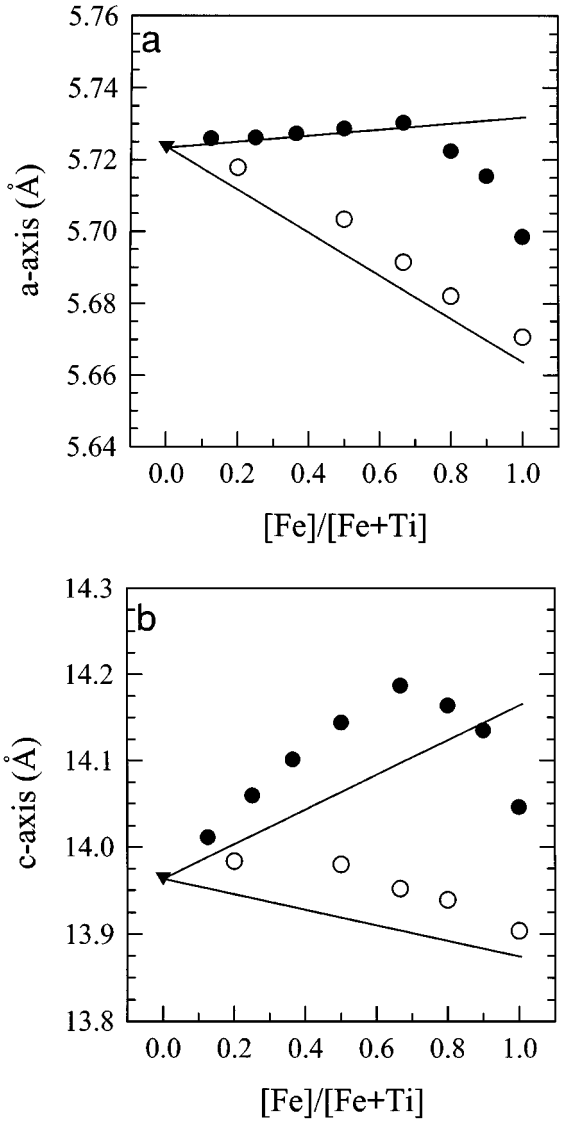

FIG. 2. Cell parameters *vs* [Fe]/[Fe+Ti] atomic ratio for air-quenched (filled circles) and slow-cooled in oxygen (open circles) samples. Filled triangles are for 6H–$BaTiO_3$ from Ref. (4). The lines correspond to Vegard-law cell composition relationships for $BaTiO_3$–$BaFeO_{2.5}$ (upper lines) and $BaTiO_3$–$BaFeO_3$ (lower lines).

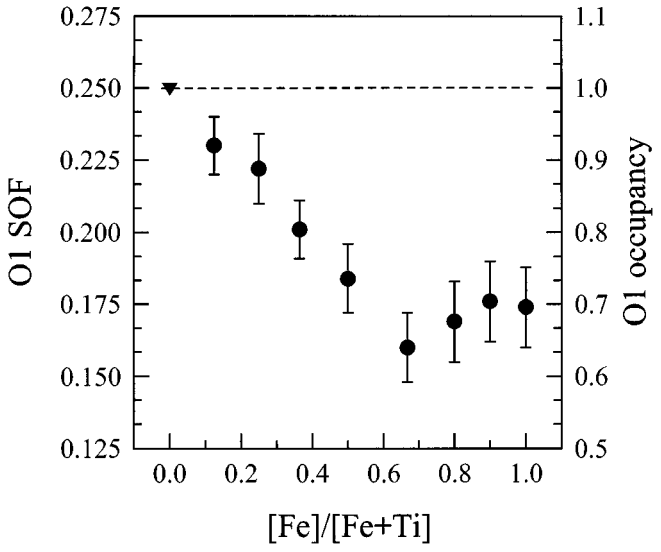

FIG. 3. Site occupation fraction (SOF) for O(1) vs [Fe]/[Fe + Ti] atomic ratio for quenched samples. Error bars represent ±2 e.s.d. The dashed line represents full occupancy of O(1), SOF = 0.25.

redistribution of some oxygen vacancies from the O(1) site to the O(2) site at high iron contents. We were unable to confirm directly the presence of vacancies at the O(2) site because the refined SOF for O(2) did not deviate significantly from full occupancy. However a ND study on 6H–$BaFeO_{2.79}$ by Jacobson (11) concluded that there was a low concentration of oxygen vacancies at the O(2) site (5% vacancies at O(2) cf. 16% vacancies at O(1)). Thus, while in 6H–$BaFeO_{3-\delta}$ there are oxygen vacancies in both the c–$BaO(2)_3$ layers and the h-$BaO(1)_3$ layers, our study suggests that substitution of titanium into the structure causes the vacancies to be localized in the h-$BaO(1)_3$ layers only. An analogous localization of unoccupied oxygen sites in the mirror planes at $z = \pm 1/4$ has been reported in 6H–Ba_2ScAlO_5 from a single crystal XRD refinement (12).

Variations in Interatomic Distances

The variations of atomic coordinates across the full composition range for the quenched and slow-cooled samples are reported in Tables 1 and 2, respectively. The variations in interatomic distances as a result of the changes in atomic coordinates and unit cell parameters are plotted as a function of the [Fe]/[Fe + Ti] ratio in Fig. 4 (M–O and M–M), Fig. 5 (Ba–M), and Fig. 6 (Ba–Ba). A comparison of Figs. 4 to 6 reveals that the M–O distances show relatively small compositional variations, while the M–M, Ba–M, and Ba–Ba separations show a range of compositional dependencies, with some distances varying strongly and others remaining almost constant. The largest variations in interatomic distances are associated with pairs of $M(2)$ atoms and/or Ba(2) atoms aligned along [001].

To understand the origins of these variations it is instructive to first consider the metal atom (Ba + M) packing in the 6H structure and then analyze the changes in interatomic interactions between the metal atoms as oxygen is removed from the O(1) site. The crystal chemistry insights gained from considering the metal atom packing in inorganic compounds and minerals were described in the 1970s by Lebedev (13). This approach has been further developed by O'Keeffe and Hyde (14) and Vegas (15).

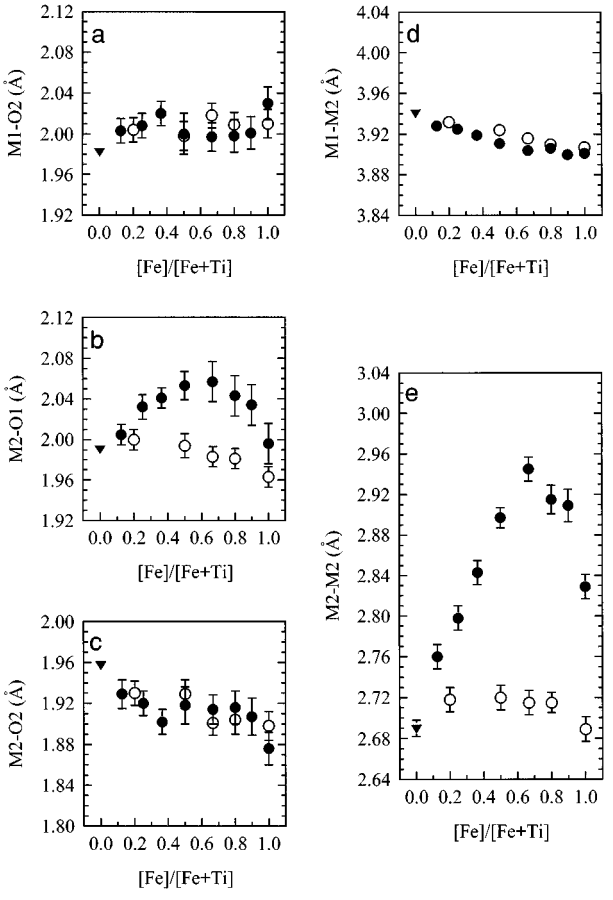

FIG. 4. M–O and M–M distances vs [Fe]/[Fe + Ti] atomic ratio for air-quenched (filled circles) and slow-cooled in oxygen (open circles) samples. Filled triangles are for 6H–$BaTiO_3$ from Ref. (4). Error bars represent ± 2 e.s.d.

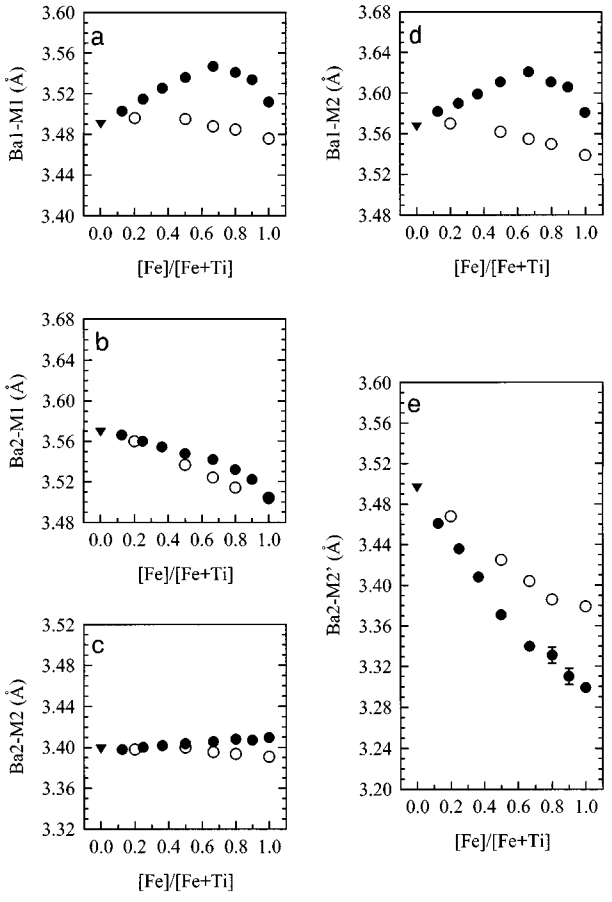

FIG. 5. Ba–M distances vs [Fe]/[Fe + Ti] atomic ratio for air-quenched (filled circles) and slow-cooled in oxygen (open circles) samples. Filled triangles are for 6H–$BaTiO_3$ from Ref. (4). Error bars represent ± 2 e.s.d.

Ba + M Metal Atom Array in 6H–$BaMO_3$

As shown in Fig. 1, the 6H–BaMO_3 type structure can be considered regularly twinned cubic BaMO_3 perovskite in which the twin composition plane is every third BaO_3 layer, parallel to $(111)_c$. This becomes the h-BaO_3 layer in the 6H phase.

Considering the metal atom packing, in cubic BaMO_3 the Ba and M atoms form interpenetrating primitive cubic arrays such that each metal atom type is at the body center of the array formed by the other metal atom type, giving octahedral coordination by like metal atoms and cubic coordination by unlike atoms. This is the structure of CsCl and β-brass, CuZn (16). The alloy BaZn has this structure, with the nearest neighbor Ba–Zn separation = 3.54 Å and with Ba–Ba (and Zn–Zn) separations of 4.09 Å. This structure type has not been reported for BaTi, but from a comparison of the unit cells for Ti and Zn metals, the corresponding Ba–Ti separation would be expected to be 3.58 Å.

Twinning of the BaM array about $(111)_c$ planes, as occurs in the 6H–BaMO_3 structure, produces two nonequivalent Ba and M atoms. A [110] projection of the BaM array, and the coordination of the Ba atoms by Ba and M atoms are illustrated in Fig. 7. Ba(1) in the twin plane retains sixfold coordination to Ba and eightfold coordination to M, as in cubic $BaTiO_3$, but the coordination geometry is changed from octahedral and cubic to trigonal prismatic and flattened, end-capped trigonal prismatic, respectively. Ba(2), in the cubic perovskite part of the structure, has its coordination number to Ba increased from 6 to 7 (capped octahedron) and its coordination number to M decreased from 8 to 7 (cube with one corner removed).

There is no change to the coordination geometry of $M(1)$, in the center of the cubic perovskite blocks, whereas $M(2)$, which lies on either side of the twin plane, has its coordination number of M reduced from 6 to 4 (flattened tetrahedron) and its coordination number to Ba decreased from 8 to 7. This reduction in the number of nonbonded M and Ba neighbors of $M(2)$ may explain the higher stability of the

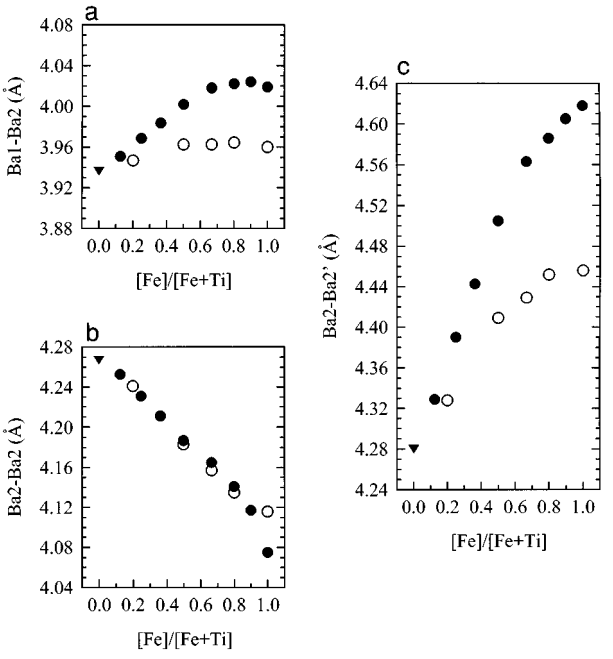

FIG. 6. Ba–Ba distances vs [Fe]/[Fe + Ti] atomic ratio for air-quenched (filled circles) and slow-cooled in oxygen (open circles) samples. Filled triangle are for 6H–$BaTiO_3$ from Ref. (4). Error bars represent ± 2 e.s.d.

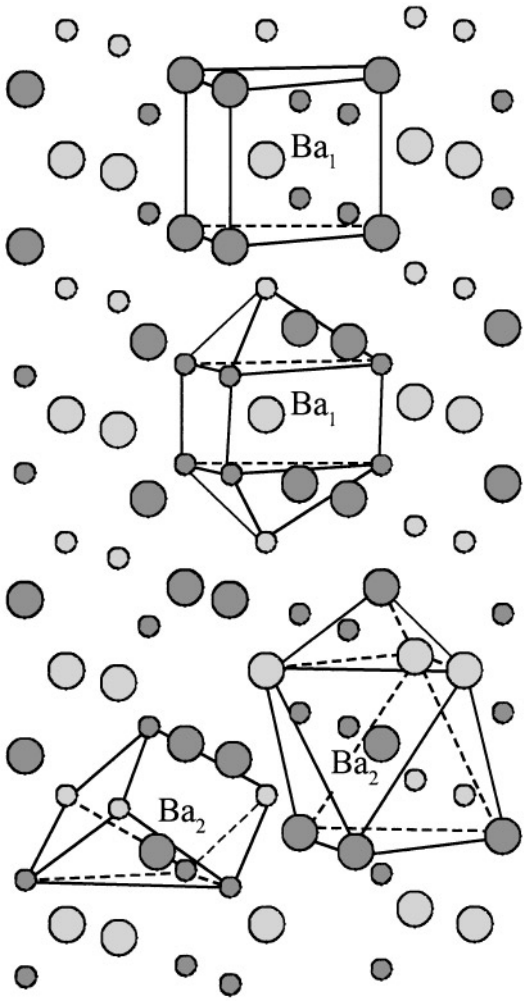

FIG. 7. Ba and *M* cation array in 6H–$BaMO_3$, viewed slightly tilted from [110], with the [001] direction vertical. Large light and heavy shaded circles are Ba(1) and Ba(2), while small light and heavy shaded circles are *M*(1) and *M*(2) respectively. Coordination polyhedra of Ba and M atoms around Ba(1) and Ba(2) are shown.

6H-perovskite relative to cubic perovskite at high temperature ($\equiv$ low pressure). A consideration of first-neighbor coordination of the metal atoms by oxygen cannot explain the relative stabilities, as the coordination numbers are unchanged from the cubic to the hexagonal perovskites. Within the context of a metal atom packing description of the 6H structure, the oxygen atoms can be considered as occupying interstitial sites in the metal atom array and contributing to the stability of the structure by relieving the strain due to strong, nonbonded repulsive forces, particularly between the *M*(2) atoms. We now consider the variations to the metal atom separations brought about by selectively removing oxygen atoms from the O(1) sites in 6H–Ba(Ti, Fe)$O_{3-\delta}$.

Variation of M(2)–M(2) in 6H–Ba(Ti, Fe)$O_{3-\delta}$

The *M*(2)–*M*(2) separation is clearly influenced by the concentration of O(1) site vacancies in the layer separating the *M*(2) atoms. As shown in Fig. 4e, the *M*(2)–*M*(2) distance increases steeply with increasing O(1) vacancy concentration, from 2.690(4) Å in $BaTiO_3$ (no vacancies) to a maximum of 2.945 Å at [Fe]/[Fe + Ti] = 0.67. Thus, as oxygens are removed from the shared octahedral face of the $M(2)_2O_9$ dimers, the cations are less well shielded and move apart as a result of the greater repulsive forces. At the composition with [Fe]/[Fe + Ti] = 0.67, one oxygen per shared octahedral face has been removed. If the unoccupied oxygen sites are uniformly distributed, the pairs of face-shared octahedra are converted to pairs of edge-shared square pyramids of composition $M(2)_2O_8$. The observed *M*(2)–*M*(2) separation of 2.945(6) Å at [Fe]/[Fe + Ti] = 0.67 compares well with the *M*–*M* separation across a shared octahedral edge of 2.92 Å in Fe_2TiO_5 (17). At values of [Fe]/[Fe + Ti] greater than 0.67, the *M*(2)–*M*(2) distance decreases with increasing iron content. The major causes for this decrease are considered to be a decrease in the amount of the large Fe^{3+} cation (the quenched iron end member analyzed to give $Fe^{3+}_{0.64}Fe^{4+}_{0.36}$) and an increase in the shielding of the *M*(2) cations due to lower vacancy concentrations at the O(1) site (see Fig. 3).

In contrast to the steep maximum observed for *M*(2)–*M*(2) in the quenched samples, the corresponding plot of *M*(2)–*M*(2) for the slow-cooled samples shows a broad,

shallow maximum with the variation in $M(2)$–$M(2)$ little greater than experimental error. This is consistent with the low levels of Fe^{3+} (and corresponding oxygen vacancies) in the slow-cooled samples, and shows that the replacement of Ti^{4+} by Fe^{4+} in the face-shared octahedra has only a small effect on the $M(2)$–$M(2)$ repulsion.

Variation of Ba–Ba and Ba–M in 6H–Ba(Ti, Fe)$O_{3-\delta}$

An important clue to the variations in metal atom separations is the observed constancy of the Ba(2)–$M(2)$ separation with change of composition, as shown in Fig. 5c. The change in this distance is only ± 0.01 Å over the full [Fe]/[Fe + Ti] range and for both quenched and slow-cooled samples. For the $BaTiO_3$ end member, the Ba(2)–Ti(2) separation (3.40 Å) is shorter than that calculated for BaTi alloy (3.58 Å). This interatomic separation is expected to be strongly resistant to further contraction. Thus, as vacancies are introduced at the O(1) site and the $M(2)$ atoms undergo strong repulsion, the Ba(2) atoms are forced to move in harmony with the $M(2)$ atoms to avoid further contraction of Ba(2)–$M(2)$. This correlated movement of the Ba(2) and $M(2)$ atoms parallel to [001] explains the large decrease in Ba(2)–$M(2)'$ (Fig. 5e) and the large increase in Ba(2)–Ba(2)′ (Fig. 6c) with variation in [Fe]/[Fe + Ti] ratio in the range 0.0 to 0.67. The shorter nonbonded distance tolerated for Ba(2)–$M(2)'$ compared with Ba(2)–$M(2)$ can be explained by the more effective shielding between Ba(2) and $M(2)'$ by the intervening $O(2)_3$ octahedral face than that provided by the partially occupied $O(1)_{4/3}O(2)$ octahedral face lying between Ba(2) and $M(2)$.

As the [Fe]/[Fe + Ti] ratio increases beyond 0.67, the changes in the Ba(2)–$M(2)'$ and Ba(2)–Ba(2)′ distances continue in the same directions, albeit at lower levels, even though there are no further increases in O(1) vacancy concentration, and the $M(2)$–$M(2)$ separation progressively decreases. However, the main driving force for the continuing monotonic Ba(2) displacement probably remains the stong resistance to contraction of the Ba(2)–$M(2)$ distance.

Structure Relaxation in the Quenched Phases

During studies on the quenched phase, it was noted that some hours after fine grinding the high iron-containing samples for PXRD measurements, small shoulders developed on the low-angle side of the peaks with high l indices. These shoulders developed progressively with time, at the expense of the main peaks. When the PXRD pattern of one of the quenched samples, with [Fe]/[Fe + Ti] = 0.67, was recollected after 4 months, it was found that the shoulders had completely replaced the original peaks. The new pattern was indexed using a hexagonal cell similar to the original cell, but with an increase in the c parameter from 14.2 to 14.4 Å. Rietveld refinement gave a relatively poot fit because of anisotropic line broadening for the (00l) reflections. The refinement results are summarized in Table 1.

The major structural changes accompanying the relaxation of the quenched structure are increases in the $M(2)$–$M(2)$ and Ba(2)–Ba(2) distances along [001] from 2.95 to 3.02 Å and from 4.56 to 4.81 Å, respectively. The origin of the structure relaxation is not clear. A possible driving force is to achieve more regular Ba–Ba coordinations. The Ba(1)–Ba(2) and Ba(2)–Ba(2) distances in freshly prepared $BaFe_{0.67}Ti_{0.33}O_{2.67}$ are 4.02 and 4.16 Å, respectively, and these two distances become equal at 4.09 Å in the relaxed structure. An alternative cause may be cooperative ordering within (00l) layers of the O(1) site vacancies. Further studies using methods such as Mossbauer spectroscopy to distinguish the local metal atom coordinations in the freshly prepared and aged, quenched samples are warranted.

Comparison with Related 6H Structures

Although there are many structural studies reported in the literature on oxygen-deficient 6H–Ba$MO_{3-\delta}$ phases, there appears to be only one other well-documented example of a 6H structure in which the oxygen vacancies are confined to the O(1) sites. This occurs for Ba_2ScAlO_5 (12), in which Sc^{3+} is ordered in $M(1)$, the $M(2)$ site comprises 0.25 Sc^{3+} + 0.75 Al^{3+}, and the O(1) sites are only half occupied. This phase shows the same structural features as the quenched, iron-rich Ba(Fe, Ti)$O_{3-\delta}$ phases, viz. strong repulsion of the $M(2)$ cations with $M(2)$–$M(2) = 3.24$ Å, a short Ba(2)–$M(2)'$ separation along [001] of 3.21 Å, and a long Ba(2)–Ba(2)′ separation along [001] of 4.86 Å. The structural similarity of Ba_2ScAlO_5 to the oxygen–deficient 6H phases reported in this study, and their difference from stoichiometric phases, is illustrated by results presented in Table 3 for a range of well-refined stoichiometric 6H phases obtained from the literature. In Fig. 8, the Ba(2)–$M(2)'$ distances for the listed phases are plotted against the mean ionic radius of the M cation. It is seen that the points for the stoichiometric phases all lie close to a linear fit, whereas the points for Ba_2ScAlO_5 and $BaFeO_{3-\delta}$ (from this study) are displaced well away from the line, with the displacement increasing with increasing oxygen vancancy content.

CONCLUSIONS

The 6-layer hexagonal perovskite 6H–$BaTiO_3$ can undergo extensive substitution of titanium by both Fe^{3+} and Fe^{4+}, forming solid solutions with the general formula $BaTi_{1-x-y}Fe_x^{3+}Fe_y^{4+}O_{3-x/2}$, where the Fe^{3+}/Fe^{4+} ratio depends on reaction temperature and gas atmosphere. Series of compounds with the majority of iron as either

TABLE 3
Comparison of Structural Parameters for $BaFeO_{2.70}$ and $BaFeO_{2.92}$ with some 6H–$BaMO_3$ Structures from the Literature

Compound	a (Å)	c (Å)	z Ba(2)	z M(2)	Occ M(1)	Occ M(2)	M(2)–M(2) (Å)	Ba(2)–M(2) (Å)	Ba(2)–M(2)′ (Å)	Ref.
Stoichiometric										
$BaCrO_3$	5.629(2)	13.698(6)	0.0925(1)	0.8465(3)	Cr^{4+}	Cr^{4+}	2.646	3.355	3.370	18
Ba_2CoRuO_6	5.7265(1)	14.0593(3)	0.08975(7)	0.84517(9)	Co^{3+}	0.25 Co^{3+} 0.75 Ru^{5+}	2.676	3.439	3.430	20
$BaTiO_3$	5.7238(7)	13.9649(7)	0.09671(5)	0.8463(1)	Ti^{4+}	Ti^{4+}	2.690	3.399	3.498	4
$Ba_3TiRu_2O_9$	5.7155(1)	14.0298(5)	0.0913(4)	0.8399(3)	0.54 Ti^{4+} 0.46 Ru^{4+}	0.23 Ti^{4+} 0.77 Ru^{4+}	2.515	3.432	3.551	21
$Ba_3YIr_2O_9$	5.885	14.627	0.093	0.840	Y^{3+}	0.5 Ir^{4+} 0.5 Ir^{5+}	2.633	3.356	3.701	19
Nonstoichiometric										
Ba_2ScAlO_5	5.7733(6)	14.530(2)	0.08269(7)	0.8615(3)	Sc^{3+}	0.25 Sc^{3+} 0.75 Al^{3+}	3.240	3.430	3.214	12
$BaFeO_{2.92}$	5.6707(1)	13.9039(2)	0.8974(9)	0.8467(2)	0.84 Fe^{4+} 0.16 Fe^{3+}	0.84 Fe^{4+} 0.16 Fe^{3+}	2.689	3.391	3.379	This work
$BaFeO_{2.70}$	5.6985(1)	14.0464(4)	0.0856(1)	0.8507(2)	0.4 Fe^{4+} 0.6 Fe^{3+}	0.4 Fe^{4+} 0.6 Fe^{3+}	2.829	3.409	3.299	This work
$BaFeO_{2.79}$	5.682(3)	13.970(5)	0.0874(6)	0.8477(3)	0.58 Fe^{4+} 0.42 Fe^{3+}	0.58 Fe^{4+} 0.42 Fe^{3+}	2.731	3.400	3.350	11

Fe^{3+} or Fe^{4+} can be prepared by quenching from high temperatures in air and by slow cooling in oxygen, respectively.

The substitution of titanium by trivalent iron is accompanied by the formation of oxygen vacancies. The results of Rietveld refinements of powder X-ray diffraction data for the samples quenched from high temperature show that the oxygen vacancies are confined to the O(1) sites that form the shared octahedral faces of binuclear M_2O_9 groups. The oxygen vacancy content increases with increasing trivalent iron substitution to a limiting composition $BaFe_{0.67}Ti_{0.33}O_{2.67}$, in which one-third of the O(1) sites are unoccupied. At [Fe]/[Fe + Ti] ratios higher than 0.67, the oxygen vacancy concentration remains constant and further incorporation of iron occurs as Fe^{4+}.

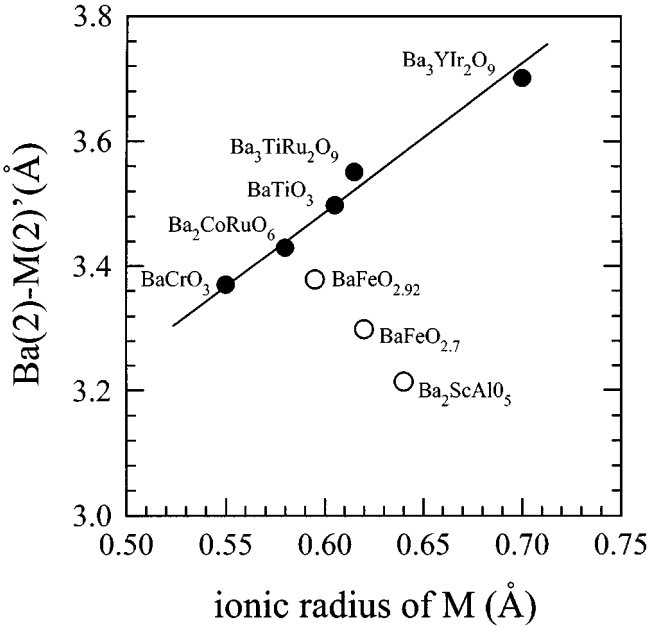

FIG. 8. Ba(2)–M(2)′ separation vs mean M ionic radius for selected 6H phases.

The major structural changes accompanying the progressive removal of oxygen from the O(1) sites are increasing M(2)–M(2) separations between metal atoms in the binuclear groups and increasing Ba(2)–Ba(2) separations along [001]. The expansion in the Ba(2)–Ba(2) distance results from the constraints imposed by strong, nonbonded Ba(2)–M(2) repulsions. A consistent interpretation of the structural changes was achieved by focusing on the M + Ba cation packing rather than the metal-centered oxide polyhedra, and by considering the changes in nonbonded repulsions as oxygen atoms are removed from interstices in the metal atom array.

Grinding the high-iron-containing quenched phases resulted in a relaxation of the structure along [001], with the c parameter expanding by 1.7%. The relaxation results in expanded M(2)–M(2) and Ba(2)–Ba(2) separations along [001] and an equalizing of the Ba(1)–Ba(2) separations.

ACKNOWLEDGMENTS

We thank Dr. B. Hyde and Dr. G. Sparrow for their constructive comments on improving the manuscript, and Ms. Lee McRae for help with some of the diagrams.

REFERENCES

1. T. A. Vanderah, J. M. Loezos, and R. S. Roth, *J. Solid State Chem.* **121,** 38 (1996).
2. I. E. Grey, L. M. D. Cranswick, and C. Li, *J. Appl. Crystallogr.*, in press.
3. R. D. Burbank and H. T. Evans, Jr., *Acta Crystallogr.* **1,** 330 (1948).
4. J. Akimoto, Y. Gotoh, and Y. Oosawa, *Acta Crystallogr. Sect. C* **50,** 160 (1994).
5. S. Mori, *J. Am. Ceram. Soc.* **49,** 600 (1966).
6. I. C. Madsen and R. J. Hill, *Adv. X-Ray Anal.* **35,** 39 (1992).
7. R. J. Hill and C. J. Howard, *J. Appl. Crystallogr.* **18,** 173 (1985).
8. D. B. Wiles and R. A. Young, *J. Appl. Crystallogr.* **14,** 149 (1981).
9. G. Caglioti, A. Paoletti, and F. P. Ricci, *Nucl. Instrum.* **3,** 223 (1958).
10. "International Tables for X-ray Crystallography," Vol. IV. Kynoch Press, Birmingham, 1974.
11. A. J. Jacobson, *Acta Crystallogr. Sect. B* **32,** 1087 (1976).
12. E. V. Antipov, R. V. Shpanchenko, L. N. Lykova, and L. M. Kovba, *Sov. Phys. Crystallogr.* **35,** 129 (1990).
13. V. I. Lebedev, *Int. Geol. Rev.* **14,** 543 (1972).
14. M. O'Keeffe and B. G. Hyde, *in* "Structures and Bonding," Vol. 61, p. 77. Springer-Verlag, Berlin, 1985.
15. L. A. Martinez-Cruz, A. Ramos-Gallardo, and A. Vegas, *J. Solid State Chem.* **110,** 397 (1994).
16. B. G. Hyde and S. Andersson, "Inorganic Crystal Structure." Wiley, New York, 1989.
17. Von P. Tiedemann and H. Muller-Buschbaum, *Z. Anorg. Allgem. Chemie.* **494,** 98 (1982).
18. B. L. Chamberland, *J. Solid State Chem.* **48,** 318 (1983).
19. I. Thumm, U. Treiber, and S. Kemmler-Sack, *J. Solid State Chem.* **35,** 156 (1980).
20. S. H. Kim and P. D. Battle, *J. Solid State Chem.* **114,** 174 (1995).
21. D. Verdoes, H. W. Zandbergen, and D. J. W. Ijdo, *Acta Crystallogr. Sect. C* **41,** 170 (1985).